High-ISO Long-Exposure Image Denoising Based on Quantitative Blob Characterization

Gang Wang, Carlos Lopez-Molina, and Bernard De Baets

***Abstract*— Blob detection and image denoising are fundamental, sometimes related tasks in computer vision. In this paper, we present a computational method to quantitatively measure blob characteristics using normalized unilateral second-order Gaussian kernels. This method suppresses non-blob structures while yielding a quantitative measurement of the position, prominence and scale of blobs, which can facilitate the tasks of blob reconstruction and blob reduction. Subsequently, we propose a denoising scheme to address high-ISO long-exposure noise, which sometimes spatially shows a blob appearance, employing a blob reduction procedure as a cheap preprocessing for conventional denoising methods. We apply the proposed denoising methods to real-world noisy images as well as standard images that are corrupted by real noise. The experimental results demonstrate the superiority of the proposed methods over state-of-the-art denoising methods.**

***Index Terms*— Image denoising, real-world noise, high-ISO long-exposure images, blob detection, blob characterization, second-order Gaussian kernel.**

I. Introduction

NOISE is intrinsic to imaging systems. When generating raw data, an image sensor incorporates certain temporal noise, correlated random noise [1] and fixed pattern noise (FPN) [2], [3]. When transforming the raw data into digital images, the in-camera image signal processor performs a series of operations, e.g. demosaicing, value clipping, white balance, color adjustment, gamma correction, tone mapping, JPEG compression, etc [4]. These procedures inevitably add or increase image noise [3]. Over the past several decades, numerous methods have been proposed for image denoising [5]. Most of them assume that the occurred noise can be approximately synthesized by Poisson or/and Gaussian noise [6], [7]. Popular denoising methods include anisotropic diffusion (AD) [8], bilateral filtering (BF) [9], the non-local means (NLM) method [10], the block-matching and 3D (BM3D) filtering [11], or more recent alternatives based on convolutional neural networks [12], [13].

The denoising methods mentioned above generally work well when the image is captured with appropriate camera settings in a good light condition, or when noise adapts to well-known parameterizations. Nevertheless, real-world noise is more complex than synthetic noise, varying with different image sensors, camera settings (e.g. ISO sensitivity and exposure value) and even imaging environments. Typically, in images taken in low-light conditions, there is noise incurred by high-ISO or/and long-exposure settings [14], especially when using suboptimal settings. This type of noise is composed of signal-independent temporal noise, signal-dependent temporal noise [15], spatially correlated random noise and spatially correlated FPN [1]. It has been reported that many representative methods, including state-of-the-art ones, have limitations in removing such noise. Although there are methods that can relieve low-light imaging problems at the time of capture, such as flash/no-flash pairs [16], raw data denoising [17], low-light image enhancement [18] or multiple frame denoising [19], methods for removing real-world noise in existing images are still highly desired. In the specific case of imaging in a low-light environment, alternative denoising methods in literature include non-linear filtering [20], multi-resolution denoising [21], [22] and sparse-coding-based processing [23]. Nevertheless, few methods have addressed the noise incurred by high-ISO and long-exposure settings.

In digital photography, high-ISO and long-exposure settings are necessary for taking photos of objects in a low-light environment [16], especially when a large depth-of-field should be guaranteed. However, such settings will compound FPN, thereby entailing heavy noise. The noise will become more complex after passing through the in-camera image signal processor. Visually, the resulting noise has a significant spatial heterogeneity. An example patch of a black background affected by high-ISO and long-exposure noise is displayed in Fig. 1. It can be seen that some noisy spots are spatially non-uniform and locally isolated. In image processing, such structures differing from their surroundings in visual properties, e.g. brightness or color, are also referred to as blobs [24]. Therefore, we refer to the spatially non-uniform and locally isolated noise appearing in high-ISO long-exposure images as blob noise. Different from other types of noise, blob noise

Manuscript received April 27, 2019; revised September 16, 2019 and March 14, 2020; accepted April 2, 2020. Date of publication April 14, 2020; date of current version April 29, 2020. The associate editor coordinating the review of this manuscript and approving it for publication was Prof. Sos S. Agaian. *(Corresponding author: Gang Wang.)*

Gang Wang is with the Institute of Military Cognition and Brain Sciences, Academy of Military Medical Sciences, Beijing 100850, China, and also with KERMIT, Department of Data Analysis and Mathematical Modelling, Ghent University, 9000 Ghent, Belgium (e-mail: gang.wang@ugent.be).

Carlos Lopez-Molina is with the Departamento de Automática y Computación, Universidad Pública de Navarra, 31006 Pamplona, Spain, and also with KERMIT, Department of Data Analysis and Mathematical Modelling, Ghent University, 9000 Ghent, Belgium (e-mail: carlos.lopez@unavarra.es).

Bernard De Baets is with KERMIT, Department of Data Analysis and Mathematical Modelling, Ghent University, 9000 Ghent, Belgium (e-mail: bernard.debaets@ugent.be).

Digital Object Identifier 10.1109/TIP.2020.2986687

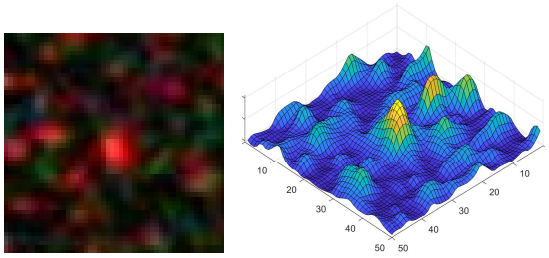

(a) (b)

Fig. 1. Image patch containing blob noise (a) and the 3D visualization of its red channel (b).

has a certain shape while occupying a certain area, and by its very nature, blob noise seriously damages the image self-similarity [10]. Conventional denoising algorithms can hardly recognize whether a structure is a noise blob or a visual image element [17]. Moreover, it is difficult to tackle blob noise in the frequency domain, since blob noise has a large number of low-frequency components that are completely mixed with true image contents [22]. These reasons make blob noise reduction a very challenging task.

In order to tackle blob noise, we propose a denoising scheme that incorporates three sequential steps: blob characterization, blob reconstruction and blob reduction. Blob detection is a fundamental image processing task and has been widely used for detecting nuclei [25], nanoparticles [26], vanishing points [27], freckles [28], etc. Over the past several decades, quite a few blob detection methods have been developed, several representative ones being the Laplacian of Gaussian (LoG) method [29], the Top-Hat (TH) method [30] and the Hessian-based LoG (HLoG) method [31]. Despite their popularity, these methods are essentially used for blob enhancement, and thus, they can hardly yield a quantitative measurement of blob characteristics. Therefore, they cannot be applied to blob reconstruction and blob reduction. Moreover, they also yield significant responses to some non-blob structures like edges and lines. Hence, we are still in need of a method that can inherently and quantitatively capture the physical characteristics of blobs, which can subsequently facilitate blob reconstruction and blob reduction.

In this paper, capitalizing on multiscale computer vision, we explore a topographical approach to characterize blobs, interpreting the image as a geographical surface. This interpretation is not new and has produced interesting methods in literature. In line detection, for example, authors use jargon like valleys or ridges to describe curvilinear structures [32]. The topographical counterpart of a blob measurement is simple: mountain measurement [33]. As displayed in Fig. 1(b), blobs can be thought of as prominent and isolated visual artifacts, which are rather close to the notion of mountains in topography. Hence, in this work, we characterize a blob using characteristics of spatial location, spatial scale and intensity prominence.

To formalize our proposal, we study the properties of the normalized second-order Gaussian kernel, and accordingly, propose a novel kernel, namely the unilateral second-order Gaussian (USOG) kernel, to obtain a quantitative measurement of blob characteristics. In the scale-space framework, the USOG kernels are normalized to yield a maximum response, which exactly reflects the blob prominence, at the scale of the observed blob. In addition, the proposed USOG kernels topographically retain the minimum response among all directions and therefore suppress non-blob structures effectively. In this way, we are able to obtain a quantitative measurement of the blob position, the scale as well as the prominence, and accordingly, we can reconstruct a blob map. Subsequently, we design a scheme to tackle blob noise in high-ISO long-exposure images, employing a blob reduction procedure as a cheap preprocessing step for conventional denoising methods. The main part of blob noise is reduced by a reconstructed blob map, while the residual noise is further removed by each of the selected conventional denoising methods, i.e. the BF method [9], the NLM method [10], the color version of block-matching and 3D filtering (CBM3D) method [11], the multi-channel weighted nuclear norm minimization (MWNNM) method [34] and the trilateral weighted sparse coding (TWSC) method [23].

This paper, which is a considerable extension of our previous work [35], is organized as follows. Section II recalls related work on real-world image denoising and blob detection. In Section III we elaborate a method to quantify blob characteristics. Subsequently, Section IV presents a denoising scheme targeting high-ISO long-exposure noise. The experimental results as well as discussions are included in Section V, while Section VI concludes this paper.

II. Related Work

In this section, we recall related work on real-world image denoising and blob detection, respectively.

A. Real-World Image Denoising

Image noise can be broadly divided into categories of temporal noise, correlated noise and FPN. Temporal noise includes thermal noise, readout noise, quantization noise, shot noise, dark current noise, etc [2], [3]. The specific causes for each type of noise vary considerably. For example, thermal noise is generated by the load resistor and renders into additive white Gaussian noise [36]. Readout noise, alternatively, is generated during the process of charge-to-voltage conversion, which is inherently inaccurate [37]. More detailed inspections for shot noise and temporal noise can be found in [36] and [38], respectively. Generally, temporal noise is usually assumed to obey Poisson or/and Gaussian distributions. However, noise in real-world images also contains correlated noise and FPN, which displays non-uniform spatial characteristics [39]. The correlated noise might be incurred by the physics of the acquisition system, the readout process, the cross-talk between neighboring pixels, or the processing performed on the raw data [39]. The major sources of FPN include dark signal non-uniformity and photon-response non-uniformity [2]. FPN will arise with the increase of ISO sensitivity or/and exposure time. Thus, FPN usually appears in images taken in a low-light environment. After passing through an image signal processor,

the noise will become very difficult to address [3]. Due to the mismatch between the actual noise characteristics and the simplified noise models, many conventional methods might underperform in removing real-world noise.

In literature, there are already some proposals for denoising images taken in low-light environments. A pioneering method is the one proposed by Rabie [20], which uses adaptive hybrid mean and median filters to attenuate stuck-pixel noise, blue-channel noise and JPEG artifacts. But this method still lacks an extensive and quantitative evaluation. The method presented in [21] classifies noise into low-frequency and high-frequency noise, and then reduces low-frequency noise by multiresolution bilateral filters. This proposal is further developed in [22], which uses the BM3D method [11] to process the down-sampled chrominance channel. Sadly, such down-sampling also leads to a loss of certain image details. Chatterjee *et al.* [40] proved that demosaicing is the main cause of random mid-frequency splotch noise, which led to a joint proposal for denoising and demosaicing. Although promising, this method is not applicable to noisy images, of which the raw data is not available. More recently, for removing noise specifically brought by high-ISO settings, Xu *et al.* [34] proposed the MWNNM method, but this method is rather time-consuming to execute. A very recent method uses the trilateral weighted sparse coding scheme (TWSC method) [23] and obtains a promising performance, but it still has limitations to address noisy patches that are quite spatially correlated. Besides, benefiting from the modelling capability of deep neural networks, some methods introduce deep learning techniques to image denoising, and have achieved state-of-the-art performance on some datasets. However, such methods might be over-fitted to the noise in the training datasets, and thus, might generalize poorly to noisy images with more complex noise [41]. Despite the works mentioned above, high-ISO long-exposure image denoising remains a challenging task.

B. Blob Detection

Blob detection is a long-standing task in image processing. Quite a few blob detection methods have been developed, and most of them rely on a signal-based interpretation. Two pioneering approaches are the LoG method [29] and Difference of Gaussian method [42], both of which are inspired by the early computational models of the human visual system. The two methods perform an intrinsic Gaussian smoothing that makes them more noise-robust than morphology-based methods, like the TH method [30] or the H-dome method [43]. For detecting blobs with heterogeneous sizes, Lindeberg [29] proposed the multiscale LoG (MLoG) method in the context of the then-new scale-space theory. The MLoG method convolves the image with a bank of kernels that covers all possible scales of blobs, yielding a maximum convolutional response at the matched scale (a.k.a. characteristic scale) for each blob [44]. Lindeberg also used the determinant of the Hessian (DoH) [29] to detect blob structures, embodying the idea that positions in the image with large and positive DoH values are likely to belong to blobs. Compared to the MLoG method, the DoH method only produces responses for regions that contain significant variations along two orthogonal directions, and therefore implies a more restrictive condition for detecting blobs than the MLoG method [45]. Elaborating on Lindeberg's work and the theory of multiscale computer vision, several other authors have presented more advanced proposals. For instance, Kong *et al.* [46] presented a method based on generalized LoG kernels (gLoG method), which estimates scales (a.k.a. sizes), shapes and orientations of the observed blobs using a bank of multiscale and anisotropic convolutional kernels, at the cost of heavy computation. Also, Zhang *et al.* proposed the HLoG method that smooths the image using LoG kernels and subsequently identifies the (overall) optimal scale using a Hessian analysis [31]. However, the HLoG method tends to underperform when the blobs in the image are heterogeneous in size.

III. Quantitative Blob Characterization

As stated earlier, existing blob detection methods are not able to yield a quantitative measurement of blob characteristics. Moreover, these methods sometimes produce significant responses to non-blob structures. To overcome these shortcomings, in this section, we study the properties of the normalized second-order Gaussian kernels in scale-space, thereby proposing the USOG kernel, which can quantitatively measure the blob characteristics.

A. Modelling a Blob Structure

Blobs have been modelled in different ways in literature. In this paper, we adopt the definition presented by Lindeberg [47], which mathematically describes a blob based on the idea that a blob would extend until it merges with another blob. Let a two-dimensional continuous signal $I : \mathbb{R}^2 \to \mathbb{R}$ obtain a local maximum $I(\mathbf{x}_0) = v_0$ at the location $\mathbf{x}_0 = [x_0, y_0]^{\mathrm{T}}$, and let $\mathbb{C}(\mathbf{x}_0)$ be a convex set that contains $\mathbf{x}_0$. For any value of the signal intensity $b \in [0, v_0[$, topographically, the protuberance surface $\mathbb{B}(\mathbf{x}; \mathbf{x}_0, b)$ is defined as follows:

$$\mathbb{B}(\mathbf{x}; \mathbf{x}_0, b) = \left\{(\mathbf{x}, I(\mathbf{x})) \mid \mathbf{x} \in \mathbb{C}(\mathbf{x}_0), \quad b \leq I(\mathbf{x}) \leq v_0\right\}, \tag{1}$$

where $\mathbf{x} = [x, y]^{\mathrm{T}}$ is the planar coordinates. Obviously, the peak point of the protuberance surface is $(\mathbf{x}_0, I(\mathbf{x}_0))$.

Since $(\mathbf{x}_0, I(\mathbf{x}_0))$ is a local maximum, in general, we can find a $b < v_0$ that results in an $\mathbb{B}(\mathbf{x}; \mathbf{x}_0, b)$ such that there exists a monotonically increasing path from any point within the set $\mathbb{B}(\mathbf{x}; \mathbf{x}_0, b)$ to the peak point $(\mathbf{x}_0, I(\mathbf{x}_0))$. Subsequently, we reduce b until we reach a b_0 such that within the resultant $\mathbb{B}(\mathbf{x}; \mathbf{x}_0, b_0)$ not all the points have a monotonically increasing path to the peak point $(\mathbf{x}_0, I(\mathbf{x}_0))$. Here, the resultant $\mathbb{B}(\mathbf{x}; \mathbf{x}_0, b_0)$ is referred to as a blob structure, while the b_0 is defined as its base level. Accordingly, the blob prominence is defined as the intensity difference between the local maximum and the base level, i.e.

$$p_0 = v_0 - b_0. \tag{2}$$

Mathematically, we assume that a blob structure has a Gaussian shape [48]. Based on the aforementioned definition of a blob structure as well as its characteristics, we describe

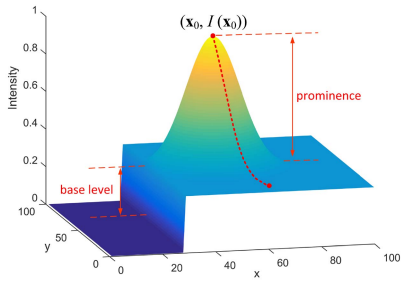

Fig. 2. Visual representation of a blob structure and its measurable characteristics.

a blob structure using four parameters: the center position, the scale, the prominence and the base level. Specifically, we formulate a blob structure as follows:

$$\Lambda(\mathbf{x};\mathbf{x}_0,\omega_0,p_0,b_0)=p_0\cdot\exp\left(-\frac{(\mathbf{x}-\mathbf{x}_0)^{\mathrm{T}}(\mathbf{x}-\mathbf{x}_0)}{2\omega_0^2}\right)+b_0, \tag{3}$$

where $\mathbf{x}_0$ denotes the center position, $p_0\in]0,\ 1]$ the prominence, $b_0\in[0,\ 1[$ the base level and ω_0 the spatial scale. As an illustration, Fig. 2 displays a blob as well as its characteristics.

In fact, the image intensity at each location is known once the image is given. Thus, according to Eq. (2), we can have b_0 once p_0 is obtained. That is, the center position, the prominence and the blob scale are sufficient to describe a modelled blob. Therefore, the blob can be delimited and reconstructed once these parameters are determined.

B. Scale-Invariant Normalized Second-Order Gaussian Kernel

The second-order Gaussian (SOG) kernel and its variants have been widely used for blob detection [46]. An SOG kernel is given by [49]

$$g''(\mathbf{x};\sigma)=\frac{x^2-\sigma^2}{2\pi\sigma^6}\exp\left(-\frac{\mathbf{x}^{\mathrm{T}}\mathbf{x}}{2\sigma^2}\right), \tag{4}$$

where $\sigma\in\mathbb{R}_+$ denotes the scale in scale-space. A directional version of an SOG kernel is created by rotating the kernel with a direction θ:

$$g''(\mathbf{x};\sigma,\theta)=\frac{\left([\cos\theta,\sin\theta]\mathbf{x}\right)^2-\sigma^2}{2\pi\sigma^6}\exp\left(-\frac{\mathbf{x}^{\mathrm{T}}\mathbf{R}_\theta^{\mathrm{T}}\mathbf{R}_\theta\mathbf{x}}{2\sigma^2}\right), \tag{5}$$

where $\mathbf{R}_\theta=[\cos\theta,\sin\theta;-\sin\theta,\cos\theta]$ is the rotation matrix.

Since the magnitude of a non-normalized Gaussian kernel (and that of its derivatives) decreases as σ increases, conventionally, the SOG kernel is normalized as follows [32]:

$$g''_{\mathrm{n}}(\mathbf{x};\sigma)=\sigma^{2\gamma}\cdot g''(\mathbf{x};\sigma). \tag{6}$$

where $\gamma\in\mathbb{R}_+$ is referred to as the scale normalization factor.

Although having gained popularity, conventionally normalized SOG kernel also produces significant responses to some non-blob structures, which will be illustrated in Section V. Moreover, the relationship between the obtained response and the true blob prominence is implicit, thereby leading to failures of blob reconstruction and blob reduction. For this reason, we intend to design a kernel that can yield a quantitative measurement of blob characteristics. Inspired by the normalization method in Eq. (6), we normalize the SOG kernel as follows:

$$\tilde{g}''_{\mathrm{n}}(\mathbf{x};\sigma)=(-1)^{\eta}\cdot\beta\cdot\sigma^{2\gamma}\cdot g''(\mathbf{x};\sigma), \tag{7}$$

where β is a constant ensuring that the obtained prominence measurement precisely reflects the original blob prominence, while $\eta\in\{0,1\}$ allows the kernel to be applicable to both bright ($\eta=1$) and dark ($\eta=0$) blob detection. In this paper, we address the detection of bright blobs, thus setting $\eta=1$.

To obtain the response of the SOG kernel to a blob, we convolve $\tilde{g}''_{\mathrm{n}}(\mathbf{x};\sigma)$ with the blob in Eq. (3). The resulting response in the center position of the blob is given by:

$$\begin{aligned}B&=\tilde{g}''_{\mathrm{n}}(\mathbf{x};\sigma)*\Lambda(\mathbf{x};\mathbf{x}_0,\omega_0,p_0,b_0)\,|_{\mathbf{x}=\mathbf{x}_0}\\&=\beta p_0\sigma^{2\gamma-2}\omega_0^2(\omega_0^2+\sigma^2)^{-1}\left[1-\omega_0^2(\omega_0^2+\sigma^2)^{-1}\right].\end{aligned} \tag{8}$$

In order to identify the scale of the blob, we intend to find the σ that yields a maximum response in scale-space [50]. For $\sigma\in\mathbb{R}_+$, it is easy to verify that the second-order derivative of B w.r.t. σ is negative. Hence, we determine the maximum value of B in scale-space by computing the first derivative of B w.r.t. σ and setting it to zero. After a few algebraic manipulations, we find that B reaches its maximum value at the scale:

$$\sigma^*=\gamma^{\frac{1}{2}}(2-\gamma)^{-\frac{1}{2}}\omega_0. \tag{9}$$

Substituting the σ in Eq. (8) by that in Eq. (9), we obtain the maximum response in scale-space:

$$B^*=\frac{\beta p_0\gamma}{4(2-\gamma)^{\gamma-2}}\omega_0^{2\gamma-2}. \tag{10}$$

In order to make the normalized SOG kernel scale-invariant, i.e. B^* is independent from ω_0, we set $\gamma=1$. Accordingly, Eq. (9) becomes $\sigma^*=\omega_0$, while Eq. (10) becomes

$$B^*=\frac{1}{4}\beta p_0. \tag{11}$$

To make the obtained response precisely reflect the blob prominence, i.e. $B^*=p_0$, we set $\beta=4$.

Eventually, taking Eq. (7) and the discussion above into consideration, we get the scale-invariant normalized SOG kernel as follows:

$$\tilde{g}''_{\mathrm{n}}(\mathbf{x};\sigma)=-4\sigma^2\cdot g''(\mathbf{x};\sigma). \tag{12}$$

To illustrate the effectiveness of the normalized SOG kernel in blob characterization, we model a blob based on Eq. (3), setting $\omega_0=4$, $p_0=0.8$ and $b_0=0.1$, as displayed in Fig. 3(a). Subsequently, we convolve $\tilde{g}''_{\mathrm{n}}(\mathbf{x};\sigma)$ with the modelled blob. The black curve in Fig. 3(b) illustrates the responses obtained at the blob center in scale-space. According to Eq. (8), the theoretical responses obtained at the blob center are supposed to follow the red curve in Fig. 3(b). As can be seen, the obtained responses agree with the theoretical values very well. Moreover, in scale-space, the normalized SOG kernel obtains its maximum value at the scale of 4, which is identical to the scale of the modelled blob. Furthermore,

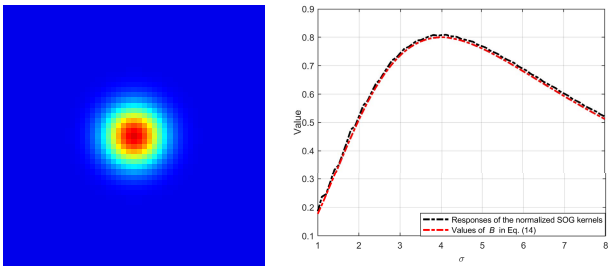

(a) (b)

Fig. 3. Illustration of a modelled blob and the obtained responses at the blob center. (a) A modelled blob ($\omega_0 = 4$, $p_0 = 0.8$ and $b_0 = 0.1$); (b) The responses yielded by the normalized SOG kernels in scale-space and the analytical values of B obtained by varying σ in scale-space ($\gamma = 1$, $\beta = 4$).

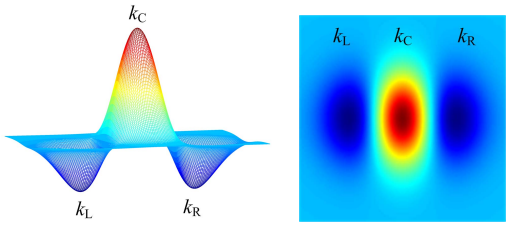

(a) (b)

Fig. 4. Three-dimensional and planar representations of a normalized SOG kernel.

the maximum response of $\tilde{g}_n''(\mathbf{x};\sigma)$ is 0.8, which equals the prominence of the modelled blob.

We are now in a position to summarize that the scale-invariant normalized SOG kernels yield the maximum response at the location $\mathbf{x}_0$ and at the scale ω_0. Moreover, the maximum response B^* precisely reflects the blob prominence p_0, regardless of the blob scale.

C. The Unilateral Second-Order Gaussian Kernel

We premise the discussion above on the assumption that the blob structure has a flat surrounding background. In fact, blobs are usually situated adjacent to other image structures. That is, the intensity differences in different directions are not always identical. According to the definition of blob prominence in Section II, we need to find the prominence as the minimum intensity difference among all directions. For this purpose, we propose to use the USOG kernel, which inherits the aforementioned merit of the scale-invariant normalized SOG kernel, to obtain the intensity difference along each direction.

According to Eqs. (5) and (12), the directional version of the scale-invariant normalized SOG kernel is given by:

$$\tilde{g}_n''(\mathbf{x};\sigma,\theta) = 2\frac{\sigma^2 - \left([\cos\theta, \sin\theta]\mathbf{x}\right)^2}{\pi\sigma^4}\exp\left(-\frac{\mathbf{x}^{\mathrm{T}}\mathbf{R}_{-\theta}\mathbf{R}_{\theta}\mathbf{x}}{2\sigma^2}\right). \tag{13}$$

We illustrate such a kernel in Fig. 4. From Eq. (13) and Fig. 4, we see that a scale-invariant normalized SOG kernel spatially consists of three parts, i.e. a central part k_C as well as two symmetrical side parts k_L and k_R. Each of them can be expressed as an individual kernel, leading to:

$$\begin{aligned}
&k_C(\mathbf{x};\sigma,\theta)\\
&\quad= \begin{cases} \tilde{g}_n''(\mathbf{x};\sigma,\theta), & \text{if } \tilde{g}_n''(\mathbf{x};\sigma,\theta) > 0\\ 0, & \text{otherwise}\end{cases}\\
&k_L(\mathbf{x};\sigma,\theta)\\
&\quad= \begin{cases} \tilde{g}_n''(\mathbf{x};\sigma,\theta), & \text{if } \tilde{g}_n''(\mathbf{x};\sigma,\theta) < 0 \text{ and } x < -y\tan\theta\\ 0, & \text{otherwise}\end{cases}\\
&k_R(\mathbf{x};\sigma,\theta)\\
&\quad= \begin{cases} \tilde{g}_n''(\mathbf{x};\sigma,\theta), & \text{if } \tilde{g}_n''(\mathbf{x};\sigma,\theta) < 0 \text{ and } x > -y\tan\theta\\ 0, & \text{otherwise.}\end{cases}
\end{aligned} \tag{14}$$

Note that $k_L(\mathbf{x};\sigma,\theta)$ and $k_R(\mathbf{x};\sigma,\theta)$ have the same sign, while $k_C(\mathbf{x};\sigma,\theta)$ has the opposite one.

As a matter of fact, the kernel $\tilde{g}_n''(\mathbf{x};\sigma,\theta)$ measures the intensity difference between the central part and its two side parts, i.e. the average of the intensity difference on both sides along the direction θ. As a result, traditional SOG kernels usually lead to a great loss of directional information, since they always bind the two side parts together. In order to measure the blob prominence defined in Section 2, we propose the unilateral second-order Gaussian kernel as follows.

For a given scale σ, the USOG kernel along the direction θ is defined by

$$\begin{aligned}
u(\mathbf{x};\sigma,\theta) = k_C(\mathbf{x};\sigma,\theta) + 2\lambda(\mathbf{x})k_L(\mathbf{x};\sigma,\theta)\\
+2(1-\lambda(\mathbf{x}))k_R(\mathbf{x};\sigma,\theta),
\end{aligned} \tag{15}$$

where

$$\lambda(\mathbf{x}) = \begin{cases} 1, & \text{if } |k_L(\mathbf{x};\sigma,\theta) * I_p(\mathbf{x})| > |k_R(\mathbf{x};\sigma,\theta) * I_p(\mathbf{x})|\\ 0, & \text{otherwise,}\end{cases} \tag{16}$$

where $I_p(\mathbf{x})$ is the image patch centered on $\mathbf{x}$ with the same size of $u(\mathbf{x};\sigma,\theta)$. As an illustration, Fig. 5 shows a three-dimensional appearance of an USOG kernel.

To make the filtering more efficient, we develop an equivalent implementation, convolving the SOG kernel with the signal as follows:

$$\begin{aligned}
&B(\mathbf{x};\sigma,\theta)\\
&\quad= I(\mathbf{x}) * u(\mathbf{x};\sigma,\theta)\\
&\quad= \lambda(\mathbf{x})\big[(k_C(\mathbf{x};\sigma,\theta) + 2k_L(\mathbf{x};\sigma,\theta)) * I(\mathbf{x})\big]\\
&\qquad+ (1-\lambda(\mathbf{x}))\big[\big(k_C(\mathbf{x};\sigma,\theta) + 2k_R(\mathbf{x};\sigma,\theta)\big) * I(\mathbf{x})\big],
\end{aligned} \tag{17}$$

where

$$\lambda(\mathbf{x}) = \begin{cases} 1, & \text{if } (-k_L(\mathbf{x};\sigma,\theta) + k_R(\mathbf{x};\sigma,\theta)) * I(\mathbf{x}) > 0\\ 0, & \text{otherwise.}\end{cases} \tag{18}$$

Obviously, in this way, the directions uniformly selected from the range of $[0, \pi[$ are able to cover all possible directions.

D. Topographical Measurement of Blob Characteristics

In order to accommodate the proposed USOG kernels to digital image processing, discrete versions of these kernels

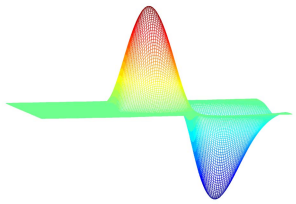

Fig. 5. Three-dimensional illustration of a USOG kernel.

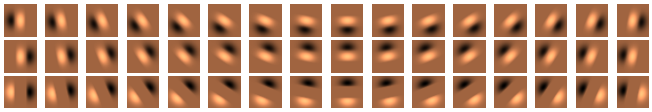

Fig. 6. A bank of kernels that is used to generate USOG kernels at a specific scale. The top row shows $(k_{\mathrm{C}}+2k_{\mathrm{L}})$, the middle row shows $(k_{\mathrm{C}}+2k_{\mathrm{R}})$ and the bottom row shows $(-k_{\mathrm{L}}+k_{\mathrm{R}})$. The intensity range of each patch has been adjusted for a better display.

are needed. We get the discrete SOG kernel by sampling the formula in Eq. (13) in the 2D integer coordinates:

$$\tilde{g}_{\mathrm{n}}''(\mathbf{m};\sigma_i,\theta_j) = 2\frac{\sigma_i^2-\left([\cos\theta_j,\sin\theta_j]\mathbf{m}\right)^2}{\pi\sigma_i^4}\exp\left(-\frac{\mathbf{m}^{\mathrm{T}}\mathbf{R}_j^{\mathrm{T}}\mathbf{R}_j\mathbf{m}}{2\sigma_i^2}\right) \quad (19)$$

where $\mathbf{R}_j=[\cos\theta_j,\sin\theta_j;-\sin\theta_j,\cos\theta_j]$ denotes the rotation matrix, $\mathbf{m}=[m_x,m_y]^{\mathrm{T}}\in\mathbb{Z}^2$ represents the discrete image coordinates, σ_i denotes the discrete scale taken from a scale set $\mathbb{S}$, and θ_j stands for the discrete direction taken from a direction set $\mathbb{D}$.

According to the expression of an SOG kernel in Eq. (19), we can easily obtain the discrete USOG kernel $u(\mathbf{m};\sigma_i,\theta_j)$ by Eqs. (14), (15) and (16). Figure 6 displays the kernels that are used to generate USOG kernels at a specific scale.

We obtain the response of the discrete USOG kernel as follows:

$$B(\mathbf{m};\sigma_i,\theta_j)=u(\mathbf{m};\sigma_i,\theta_j)*I(\mathbf{m}). \quad (20)$$

According to the definition of the blob prominence in Section 2, at each scale, the minimum response among all the directions is selected as the scale blob prominence. Therefore, at a give scale σ_i, the blob prominence is represented by

$$B(\mathbf{m};\sigma_i)=\min_{\theta_j\in\mathbb{D}} B(\mathbf{m};\sigma_i,\theta_j). \quad (21)$$

Subsequently, the maximum blob prominence in scale-space is retained as the final blob prominence:

$$B(\mathbf{m})=\max_{\sigma_i\in\mathbb{S}} B(\mathbf{m};\sigma_i). \quad (22)$$

We then identify the positions of the blobs as the local maximizers of $B(\mathbf{m})$, and thereby obtaining the map of blob prominence based on the responses at these positions.

With respect to the scale information, as stated earlier, the response in scale-space reaches its maximum value at the scale of the original blob scale. Hence, the scale of each blob is identified by

$$S(\mathbf{m})=\arg\max_{\sigma_i\in\mathbb{S}} B(\mathbf{m};\sigma_i). \quad (23)$$

Consequently, we obtain the blob characterization method based on the unilateral second-order Gaussian kernel (USOG method) to quantitatively measure the blob characteristics, including the position, the prominence and the scale.

IV. High-ISO Long-Exposure Image Denoising

Having proposed a method to quantitatively measure blob characteristics, in this section, we intend to tackle the problem of high-ISO long-exposure image denoising, which has been rarely addressed in literature. We firstly present an approach to model high-ISO long-exposure noise. Subsequently, we propose a denoising scheme by employing a step of blob reduction as a preprocessing step for five selected conventional denoising methods, i.e. the BF [9], NLM [10], CBM3D [11], MWNNM [34] and TWSC [23] methods.

A. Spatially Modelling Blob Noise

Denoising is the process of restoring the original image by reducing the undesirable noise from a noisy image [51]. As argued earlier, real-world noise is very complex, and might combine signal-dependent noise, signal-independent noise, FPN, etc [2], apart from that induced by the own image processor. Approximately, real-world noise ζ_{rw} can be modelled by

$$\zeta_{\mathrm{rw}}(\mathbf{m})=\mathcal{D}_{\mathrm{isp}}\big(\mathcal{D}_{\mathrm{clip}}\big(\zeta_{\mathrm{sd}}\left(I_{\mathrm{t}}(\mathbf{m})\right)+\zeta_{\mathrm{si}}+\zeta_{\mathrm{scr}}(I_{\mathrm{t}}(\mathbf{m}),\mathbf{m}) +\zeta_{\mathrm{fpn}}(I_{\mathrm{t}}(\mathbf{m}),\mathbf{m})\big)\big), \quad (24)$$

where $\mathcal{D}_{\mathrm{isp}}$ denotes the degradation in the image signal processor [41], $\mathcal{D}_{\mathrm{clip}}$ represents the degradation brought by the clipping operation [14], ζ_{sd} stands for spatially uncorrelated signal-dependent noise, ζ_{si} denotes spatially uncorrelated signal-independent noise, ζ_{scr} stands for spatially correlated random noise [1], ζ_{fpn} represents spatially correlated FPN and I_{t} is the true (i.e. clean) image signal. From Eq. (24), it can be learned that modelling ζ_{rw} in the spatial space is very difficult. We simplify this problem by assuming that the blob-like artifacts in ζ_{rw} can be represented as additive blob noise. Therefore, we spatially model the degradation process brought by high-ISO long-exposure settings as a degradation function together with additive blob noise. Accordingly, we model the noisy image in the spatial domain as follows:

$$I_{\mathrm{noi}}^{(q)}(\mathbf{m})=\mathcal{D}^{(q)}\big(I_{\mathrm{t}}^{(q)}(\mathbf{m})\big)+\xi_{\mathrm{b}}^{(q)}(\mathbf{m}), \quad (25)$$

where $I_{\mathrm{noi}}^{(q)}$ $(q\in\{1,2,3\})$ denotes the q-th channel of a noisy color image, $I_{\mathrm{t}}^{(q)}$ represents the q-th channel of the true image signal, $\xi_{\mathrm{b}}^{(q)}$ stands for the additive blob noise, while $\mathcal{D}^{(q)}$ denotes a degradation process on the image imposed by other types of noise, e.g. white Gaussian noise, Poisson noise, etc. In this paper, we mainly focus on how to remove the blob noise $\xi_{\mathrm{b}}^{(q)}$. Hence, we further model the blob noise using spatially mixed Gaussian functions as follows:

$$\xi_{\mathrm{b}}^{(q)}=\sum_{\mathbf{m}_i\in I_{\mathrm{t}}^{(q)}}\mathcal{H}^{(q)}(\epsilon-\epsilon_0)G^{(q)}(\mathbf{m};\mathbf{m}_i,\hat{\sigma}_i,\hat{p}_i), \quad (26)$$

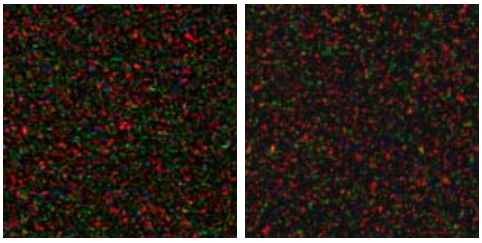

Fig. 7. Illustration of the real high-ISO long-exposure noise (left) and the modelled noise (right). Please zoom electronically for a better view.

(a) (b) (c) (d)

Fig. 8. Illustration of the process of the proposed denoising scheme. (a) A noisy image; (b) The red channel of (a); (c) Result of a blob reduction on the red-channel image; (d) The denoising result of the proposed BR-CBM3D method.

where $\mathcal{H}^{(q)}$ represents the Heaviside step function:

$$\mathcal{H}^{(q)}(\epsilon-\epsilon_0)=\begin{cases}0, & \text{if } \epsilon-\epsilon_0<0\\ 1, & \text{otherwise,}\end{cases} \tag{27}$$

in which ϵ denotes an argument that follows the continuous uniform distribution on the unit interval $[0, 1]$ and $\epsilon_0 \in [0, 1]$ is a constant. The term $\mathcal{H}^{(q)}$ reflects the probability of FPN occurring at a location. If FPN occurs at $\mathbf{m}_i$, the blob noise is approximated by a local blob structure $G^{(q)}$:

$$G^{(q)}(\mathbf{m};\mathbf{m}_i,\hat{\sigma}_i,\hat{p}_i)=\hat{p}_i\cdot\exp\left(-\frac{(\mathbf{m}-\mathbf{m}_i)^{\mathrm{T}}(\mathbf{m}-\mathbf{m}_i)}{2\hat{\sigma}_i^2}\right), \tag{28}$$

where $\hat{\sigma}_i$ and $\hat{p}_i$, which are both normally distributed, denote the prominence and scale, respectively. In Fig. 7, we display a blob noise map modelled by Eq. (26). Although not perfect, the modelled noise can generally reflect the appearance of real high-ISO long-exposure noise.

B. Denoising Methods Incorporating Blob Reduction

As elaborated earlier, we use the USOG method to obtain a quantitative measurement of blob characteristics, including the center position, blob prominence and spatial scale. Subsequently, according to the blob model in Eq. (3), we are able to reconstruct the blobs using the quantitative measurements. Specifically, we obtain a binary blob center map B_{lm} using the local maximizers of B. For a blob centered at the location $\mathbf{m}_i$, we can get its blob prominence $p_i = B(\mathbf{m}_i)$ and blob scale $\sigma_i = S(\mathbf{m}_i)$. Then, similar to Eq. (28), we reconstruct this blob as follows:

$$\Lambda^{(i)}(\mathbf{m})=p_i\cdot\exp\left(-\frac{(\mathbf{m}-\mathbf{m}_i)^{\mathrm{T}}(\mathbf{m}-\mathbf{m}_i)}{2\sigma_i^2}\right). \tag{29}$$

Subsequently, the aggregate of all the reconstructed $\Lambda^{(i)}$ is computed as the blob reconstruction map. In this way, for a given channel of the high-ISO long-exposure image, we can also obtain a map of reconstructed blob noise $\hat{I}_{\mathrm{b}}^{(q)}$. Then, according to Eqs. (26) and (28), we use $\hat{I}_{\mathrm{b}}^{(q)}$ as an approximation of $\xi_{\mathrm{b}}^{(q)}$. Therefore, using $\hat{I}_{\mathrm{b}}^{(q)}$, we reduce the main part of the blob noise as follows:

$$\hat{I}^{(q)}=I_{\mathrm{noi}}^{(q)}-\xi_{\mathrm{b}}^{(q)}\approx I_{\mathrm{noi}}^{(q)}-\hat{I}_{\mathrm{b}}^{(q)}. \tag{30}$$

A real-world noisy image denoising case is displayed in Fig. 8(a). The red channel of the noisy image is shown in Fig. 8(b). Figure 8(c) displays the blob reduction result based on Eq. (30). One can see that, although the result is not perfect, most of the blob noise has been reduced.

To further restore the image, we select several conventional denoising methods to reduce both the residual noise and the errors caused by the blob reduction procedure, respectively. In this paper, we adopt three widely used methods, i.e. the BF [9], NLM [10] and CBM3D methods [11], and two state-of-the-art methods, i.e. the MWNNM [34] and TWSC [23] methods. In this way, we get five denoising methods, each of which incorporates a blob reduction (BR) procedure, and accordingly, we refer to the five proposed denoising methods as the BR-BF, BR-NLM, BR-CBM3D, BR-MWNNM and BR-TWSC methods. As an example, Fig. 8(d) shows a denoising result obtained by the BR-CBM3D method.

V. Experimental Validation

We have presented the USOG method to quantitatively measure the blob characteristics. Building on this method, we have also developed a denoising scheme by employing blob reduction as a preprocessing step for five conventional denoising methods, thereby getting five denoising methods incorporating blob reduction. In this section, we test the USOG method for blob reconstruction and blob reduction on an image containing synthetic blobs and white Gaussian noise. In addition, to confirm whether or not the proposed denoising scheme can tackle the real noise occurring in high-ISO long-exposure images, we employ the developed denoising methods, i.e. the BR-BF, BR-NLM, BR-CBM3D, BR-MWNNM and BR-TWSC methods, to remove real blob noise.

A. Experiments on Removing Synthetic Blobs and Noise

To highlight the advantages of the USOG method for blob characterization, on a synthetic image, we use the proposed USOG method, which is summarized in Algorithm 1, to characterize, reconstruct and remove the blobs. Subsequently, we further remove the white Gaussian noise, using the BR-NLM method as a representative method.

The synthetic image, as shown in Fig. 9(a), contains blobs whose scales vary from 3.00 to 4.00, accompanied by some non-blob structures, like edges, bar-shaped lines, corners and terminations. The noisy synthetic image is obtained by adding Gaussian white noise with zero mean and a variance of 0.005. As for the parameter settings of the USOG method, the multiple scales are taken from 3 to 4 with a step of $1/3$, which covers the scales of the synthetic blobs, while the directions are selected from $\pi/8$ to π with a step of $\pi/8$.

Algorithm 1 The USOG Method for Blob Reconstruction and Reduction

Input: Original image I, scale set $\mathbb{S}$, direction set $\mathbb{D}$
Output: Blob reduction result $\hat{I}$

for each $\sigma_i \in \mathbb{S}$ **do**
  for each $\theta_j \in \mathbb{D}$ **do**
    $B(\mathbf{m};\sigma_i,\theta_j) \leftarrow u(\mathbf{m};\sigma_i,\theta_j) * I(\mathbf{m})$
  end for
  $B(\mathbf{m};\sigma_i) \leftarrow \min_{\theta_j\in\mathbb{D}} B(\mathbf{m};\sigma_i,\theta_j)$
end for
$B(\mathbf{m}) \leftarrow \max_{\sigma_i\in\mathbb{S}} B(\mathbf{m};\sigma_i)$
$S(\mathbf{m}) \leftarrow \arg\max_{\sigma_i\in\mathbb{S}} B(\mathbf{m};\sigma_i)$
$B_{\mathrm{lm}}(\mathbf{m}) \leftarrow$ local maximizers of $B(\mathbf{m})$
$\hat{I}_{\mathrm{b}} \leftarrow$ Blob reconstruction using $B_{\mathrm{lm}}(\mathbf{m})$, $B(\mathbf{m})$ and $S(\mathbf{m})$
$\hat{I} \leftarrow I - \hat{I}_{\mathrm{b}}$

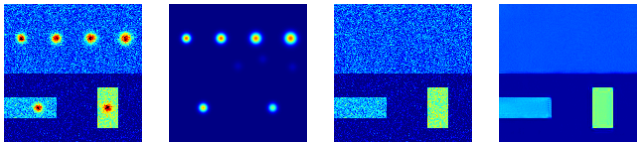

(a) (b) (c) (d)

Fig. 9. Illustration of removing synthetic blobs and noise by the proposed method. (a) Synthetic image; (b) Blob reconstruction result; (c) Blob reduction result; (d) Result of the BR-NLM method. For a better visualization, the images are displayed using the heat maps of intensity.

The blob reconstruction and blob reduction results are shown in Figs. 9(b) and 9(c). It can be seen that the blobs in the synthetic images have been reconstructed and removed successfully. Moreover, the denoising result of the BR-NLM method displayed in Fig. 9(d) demonstrates that the designed denoising scheme can remove both blobs and white Gaussian noise effectively.

For comparison, we use several widely adopted blob detection methods, including the TH, MLoG and gLoG methods, to characterize the blobs. The parameters in these methods are set according to the characteristics of the synthetic blobs and the original implementation. For reproducibility, the parameter settings of each method are listed as follows:

- TH: The morphological structuring element is set as a disk-shaped element. The scale of the structuring element is set to be 4.0 (i.e. the radius is 13 pixels).
- MLoG: The multiple scales are taken from 3.00 to 4.00 with a step of $1/3$.
- gLoG: The multiple scales are taken from 3.00 to 4.00 with a step of $1/3$. The directions are selected from $\pi/9$ to π with a step of $\pi/9$.

The responses of the different methods are shown in Fig. 10. In contrast to the response of the USOG method shown in Fig. 10(a), which has significant values only for blobs, the responses yielded by the competing methods also have significant values for non-blob structures. The TH method is sensitive to noise, while the MLoG and gLoG methods yield significant responses at locations of edges, corners, etc.

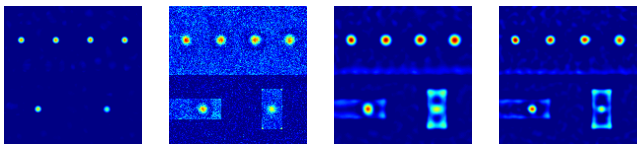

(a) (b) (c) (d)

Fig. 10. Responses obtained by the USOG method (a), the TH method (b), the MLoG method (c) and the gLoG method (d). For a better visualization, the images are displayed using the heat maps of intensity.

Therefore, these competing methods can hardly be used for precise blob characterization.

B. Experiments on Removing Real Noise

1) Experimental Setup: In this section, we test the developed denoising methods, i.e. the BR-BF, BR-NLM, BR-CBM3D, BR-MWNNM and BR-TWSC methods, to remove real high-ISO long-exposure noise. To demonstrate the effectiveness of the blob reduction, we also compare the developed denoising methods with their correspondingly original denoising methods.

In the selected conventional methods, most of the parameters are set according to the original papers. For the sake of fairness, some parameters are also optimally set by selecting the parameters that yield the best result. Specifically, to make the results reproducible, the parameter settings are listed as follows:

- BF: The degree of smoothing is optimally selected from 0.001 to 0.060 with a step of 0.001.
- NLM: The size of the similarity square neighborhood and the size of the search window are set as 7 and 21, respectively [10]. The parameter determining the filtering strength is optimally selected from 0.050 to 0.080 with a step of 0.005.
- CBM3D: The block size, the sliding step and the length of the search neighborhood are set as 8, 3 and 39, respectively [11]. The algorithm is carried out in $\mathrm{A}_{\mathrm{opp}}$ color space [52]. The standard deviation, i.e. the assumed noise intensity, is optimally selected from 1 to 50 with a step of 1.
- MWNNM: The size of local patches, the size of the search window, the number of non-local similar patches, the initial penalty parameter and the number of iterations are set as 6, 40, 70, 6 and 2, respectively [34]. The noise estimation parameter is optimally selected from 0.5 to 5.0 with a step of 0.5.
- TWSC: The size of local patches, the size of the search window, the number of similar patches, the initial penalty parameter, the penalty parameter update factor and the maximum number of iterations are set as 6, 60, 90, 0.5, 1.1 and 10, respectively [23]. The noise estimation parameter is optimally selected from 0.5 to 5.0 with a step of 0.5.

In the proposed blob reduction method, we adopt RGB color space and configure the direction set as $\mathbb{D} = \{\pi \cdot i/8 \mid i \in 1, 2, \ldots, 8\}$. The scale set is configured

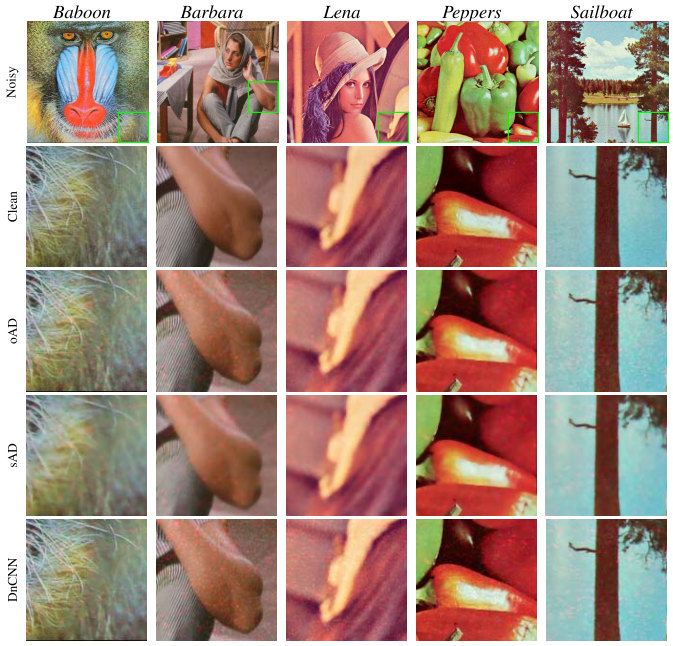

Fig. 11. Noisy standard images corrupted by real noise along with the ground truth, and the denoising results obtained by the oAD, sAD, and DnCNN methods. Please zoom electronically for a better view.

according to the size of the blob noise. For a blob noise structure having a radius r ($r \geq 3$), the corresponding kernel scale is supposed to be $(r-1)/3$. In this experiment, we configure the scale set as $\mathbb{S} = \left\{\frac{2}{3}, 1, \frac{4}{3}, \frac{5}{3}\right\}$.

When conducting experiments on standard images, we also adopt two other methods for comparison, i.e. the AD method [8] and the denoising method using deep convolutional neural networks (DnCNN) [12]. Furthermore, in the experiments of real-world image denoising, we adopt a state-of-the-art low-light image enhancement method named LECARM [53]. The parameters in the DnCNN[1] and LECARM[2] methods are set as the default values. When performing the AD methods, we set the number of diffusion iterations N_{itr} in two ways. The optimal anisotropic diffusion (oAD) method is configured with the N_{itr} that yields the best quantitative evaluation result, while the strong anisotropic diffusion (sAD) method is configured with $N_{\text{itr}} = 7$.

All the experiments are conducted in a Matlab (R2014b) environment and on a PC with Intel Core(TM) i7-3770 CPU 3.40GHz×2 and RAM 16.00GB.

2) Performance on Standard Images: We first carry out the experiments on noisy versions of the selected standard images, which are obtained by adding real high-ISO long-exposure noise. The real noise is obtained by taking black photos using a digital single-lens reflex camera with high ISO sensitivity and long exposure time. As shown in Fig. 11, the selected standard images include the *Baboon*, *Barbara*, *Lena*, *Peppers*[3] and *Sailboat*[4] (a.k.a. *Sailboat on lake*), all of which have an identical resolution 512 × 512 × 3. These images reflect a diversity of image content and are extensively used in the image processing field. In this way, we have both the ground truth clean image and noisy images, and as such, we are able to obtain a quantitative evaluation.

[1]https://github.com/cszn/DnCNN
[2]https://github.com/baidut/LECARM
[3]https://homepages.cae.wisc.edu/ ece533/images
[4]http://sipi.usc.edu/database/database.php?volume=misc

TABLE I
PSNR (dB) OF THE DENOISING RESULTS

Method	*Baboon*	*Barbara*	*Lena*	*Peppers*	*Sailboat*
oAD	26.79	28.52	28.89	27.01	28.12
sAD	23.61	26.64	28.40	26.98	26.80
DnCNN	26.39	27.96	28.47	26.87	27.89
BF	27.01	29.42	29.52	27.58	28.54
BR-BF	28.45	31.66	32.18	**31.07**	30.46
NLM	24.92	29.69	29.32	27.32	27.34
BR-NLM	25.51	31.52	31.15	30.00	28.20
CBM3D	26.94	30.03	29.46	27.32	28.19
BR-CBM3D	**28.55**	**32.59**	32.14	30.94	30.42
MWNNM	27.12	30.06	29.30	27.56	28.42
BR-MWNNM	28.44	32.31	31.91	31.02	30.41
TWSC	27.05	30.07	29.59	27.47	28.31
BR-TWSC	**28.55**	32.40	**32.27**	31.03	**30.53**

In this experiment, we adopt the widely used Peak Signal-to-Noise Ratio (PSNR) as a quantitative evaluation metric, which is defined by:

$$\text{PSNR} = 10\log_{10}\left(\frac{|I_{\text{t}}|}{\sum_{\mathbf{m}\in I_{\text{t}}}[I_{\text{t}}(\mathbf{m}) - I_{\text{d}}(\mathbf{m})]^2}\right), \qquad (31)$$

where I_{t} represents the true image, I_{d} the denoising result and $|I_{\text{t}}|$ the number of pixels in I_{t}. Note that both the I_{t} and I_{d} have been transformed into the intensity range of $[0, 1]$. For image denoising, a higher PSNR is preferred.

The obtained quantitative evaluation results are reported in Table I and the visual denoising results are shown in Figs. 11 and 12. It can be seen that all methods struggle with the complexity of the task. The oAD method, for example, cannot remove the noise effectively. Although the sAD method can attenuate the blob noise better than the oAD method, it expectedly suppresses image details, which leads to a significant decrease of the PSNR values. The DnCNN method also underperforms in removing blob noise. This is reasonable because the generalization of deep convolutional neural networks largely depends on the ability in memorizing training data, and the original DnCNN is essentially trained by images corrupted by additive white Gaussian noise [41]. Compared with the AD and DnCNN methods, the BF, NLM, CBM3D, MWNNM and TWSC methods perform slightly better in terms of PSNR and visual denoising results. However, these methods, including the TWSC method that has been designed for removing real-world noise, still have limitations in removing blob noise. In contrast, the methods incorporating blob reduction achieve a considerable performance in removing blob noise. This is confirmed on all the test images in terms of PSNR and visual denoising results, which demonstrates that the use of blob reduction can effectively benefit high-ISO long-exposure noise removal.

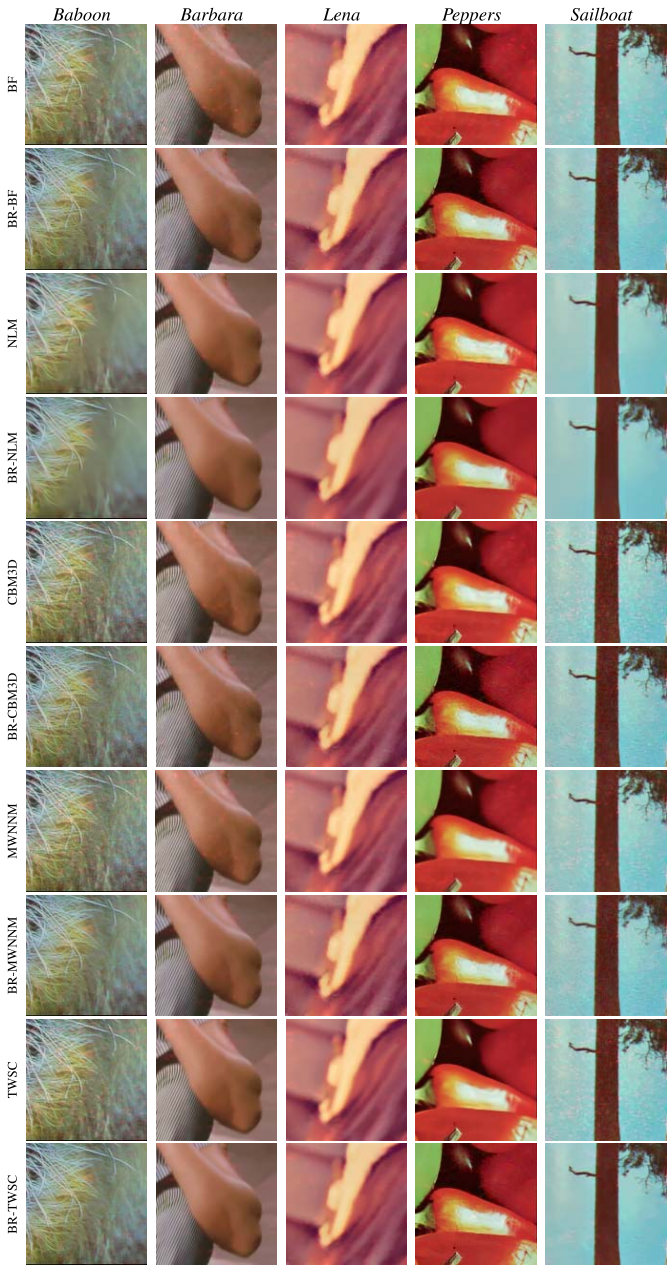

Fig. 12. Denoising results on the noisy standard images obtained by the selected conventional denoising methods and the proposed methods incorporating a blob reduction procedure. Please zoom electronically for a better view.

The execution time of each method is reported in Tab. II. The oAD, sAD and BF methods are comparatively more efficient to execute, while the MWNNM and BR-MWNNM methods are the most time-consuming among all the methods tested. Note that compared with the original denoising methods, our methods incorporating blob reduction obtain better performances at the expense of acceptable additional computation (around 2 seconds in terms of runtime). Moreover, in our method, the convolution operations performed by the proposed USOG kernels are essentially linear filtering. The filtering procedures among different kernels are mutually independent. Thus, our method can be further accelerated by parallel computing.

TABLE II
RUNTIME (S) OF EACH METHOD ON EACH IMAGE

Method	*Baboon*	*Barbara*	*Lena*	*Peppers*	*Sailboat*
oAD	0.08	0.08	0.08	0.23	0.08
sAD	0.38	0.38	0.39	0.40	0.42
DnCNN	16.54	16.51	16.52	16.63	17.05
BF	0.05	0.05	0.05	0.05	0.06
BR-BF	2.13	1.88	1.98	1.88	1.82
NLM	140.54	140.83	141.28	141.18	140.80
BR-NLM	142.65	142.11	143.49	143.22	142.07
CBM3D	4.75	4.64	5.21	5.22	5.15
BR-CBM3D	6.44	6.26	7.11	7.12	6.90
MWNNM	286.58	277.91	277.14	281.39	280.17
BR-MWNNM	288.59	279.17	278.98	283.28	281.94
TWSC	136.44	134.06	134.70	138.11	136.13
BR-TWSC	138.39	135.68	136.72	140.02	137.88

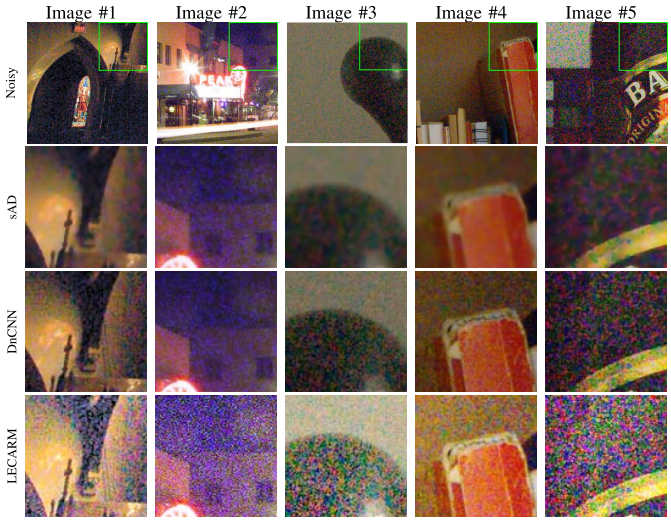

Fig. 13. Five real-world noisy images (top row) (Courtesy: Liu *et al.* [54]) and the processing results of the sAD, DnCNN and LECARM methods. Please zoom electronically for a better view.

Nonetheless, our methods still have limitations in denoising areas with plenty of textural structures. For instance, the denoising results on the image *Baboon* show a limited performance in terms of PSNR (less than 30dB). This is because the methods have to make a difficult compromise between removing more noise and preserving more structural details.

3) Performance on Real-World Images: We further apply the proposed denoising methods as well as the competing methods to real-world noisy images. As shown in Fig. 13, these noisy images are highly corrupted by high-ISO long-exposure noise that is difficult to remove by the sAD and DnCNN methods. Moreover, this type of noise can hardly be reduced by the low-light enhancement LECARM method.

The denoising results obtained by the BR-based methods as well as the original methods are displayed in Fig. 14. The original BF, NLM, CBM3D, MWNNM and TWSC methods also underperform in removing blob noise. Comparatively, the methods incorporating blob reduction yield results with better visual quality. This is consistent with the experimental

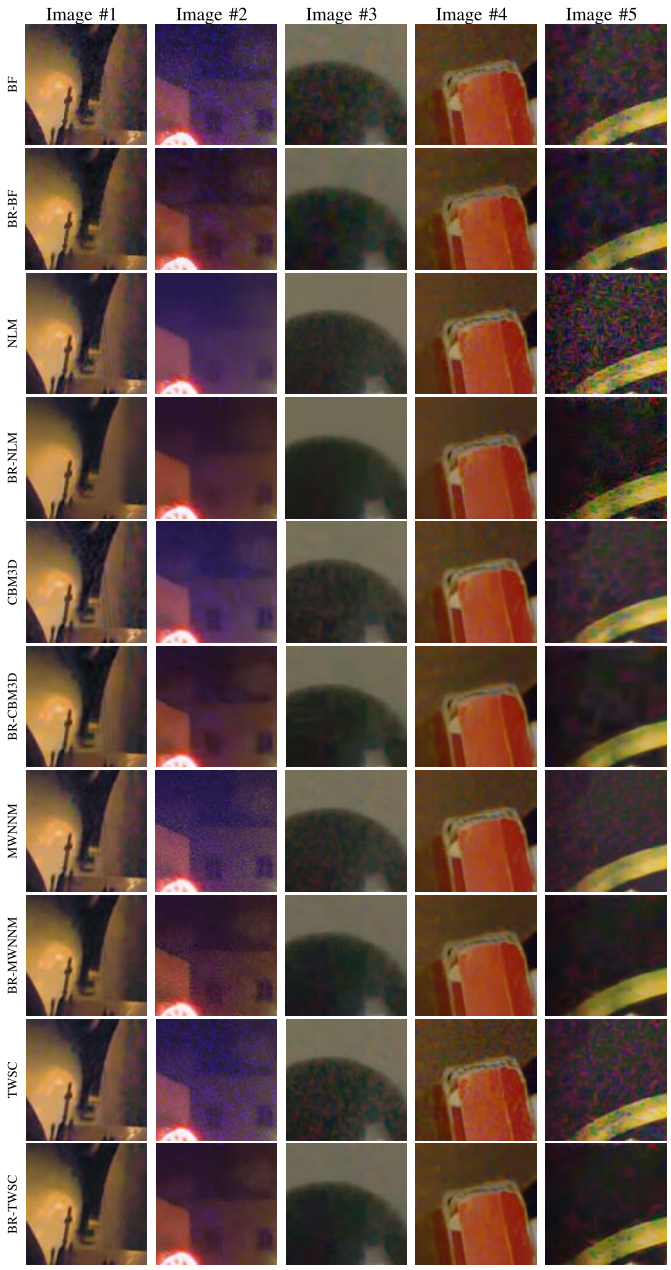

Fig. 14. Denoising results on five real-world noisy images obtained by the selected conventional denoising methods and the proposed methods incorporating blob reduction. Please zoom electronically for a better view.

results obtained on the standard images. For example, when denoising the real-world noisy Image #5 shown in the top right of Fig. 13, the original BF, NLM, CBM3D, MWNNM and TWSC methods fail in removing the heavy noise. In their denoising results, the blob noise is blurred and mingled, which damages the quality of the images. By contrast, the methods incorporating blob reduction remove more noise. This is mainly because the blob reduction procedure can significantly reduce the mass of the blob noise while retaining the image contents and structures, which highly benefits a subsequent denoising procedure. It is worth noting that our methods might underperform when FPN is extremely spatially correlated. For instance, when processing the real-world noisy

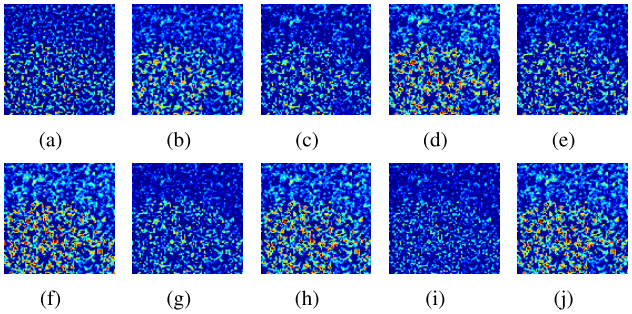

Fig. 15. Illustration of the removed noise on the real-world noisy Image #5 (red channel) obtained by the (a) BF, (b) BR-BF, (c) NLM, (d) BR-NLM, (e) CMB3D, (f) BR-CBM3D, (g) MWNNM, (h) BR-MWNNM, (i) TWSC and (j) BR-TWSC methods, respectively. For a better visualization, the images are displayed using the heat maps of intensity.

Image #5, our methods fail to remove some noisy spots. This is because such heavy noise does not agree with the assumptions of our blob characterization method.

In Fig. 15, we also show the removed noise (a.k.a. method noise [10]) obtained on the red channels of the real-world noisy Image #3 displayed in Fig. 13. These maps of the removed noise also demonstrate that the blob reduction helps remove more blob noise.

Therefore, it can be inferred that the BF, NLM, CBM3D, MWNNM and TWSC methods can benefit from the proposed blob reduction procedure in tackling high-ISO long-exposure noise. Although not providing a perfect solution, the proposed blob reduction method helps remove the high-ISO long-exposure noise in a cheap way.

VI. Conclusion and Future Work

In this paper, we have presented a computational method to quantitatively measure the blob characteristics, using the proposed unilateral second-order Gaussian kernels. This method not only identifies the blob position, the prominence and the scale, but also suppresses non-blob structures well, and as such, this method can facilitate the implementation of the blob reconstruction and blob reduction. Moreover, to tackle blob noise that occurs in high-ISO long-exposure images, we have developed a denoising scheme by employing a blob reduction procedure for each of the selected conventional denoising methods. The experimental results demonstrate that in high-ISO long-exposure image denoising, the methods incorporating blob reduction outperform the original conventional methods. Nevertheless, the proposed blob reduction method is still based on low-level features, and thus, it might undermine some semantic objects appearing like blob noise. One possible solution is to use a deep-learning-based object detector to indicate small semantic objects, which will be excluded in a subsequent blob reduction procedure. Another potential solution is to train a deep neural network with synthetic noisy images corrupted by real-world blob noise and synthetically modelled blob noise. Furthermore, more advanced applications of the proposed blob characterization method, e.g. astronomical image denoising and adjacent blob separation, will also be among future work.

REFERENCES

[1] M. Maggioni, E. Sanchez-Monge, and A. Foi, "Joint removal of random and fixed-pattern noise through spatiotemporal video filtering," *IEEE Trans. Image Process.*, vol. 23, no. 10, pp. 4282–4296, Oct. 2014.

[2] J. Xu, L. Zhang, and D. Zhang, "External prior guided internal prior learning for real-world noisy image denoising," *IEEE Trans. Image Process.*, vol. 27, no. 6, pp. 2996–3010, Jun. 2018.

[3] Y. Tsin, V. Ramesh, and T. Kanade, "Statistical calibration of CCD imaging process," in *Proc. 8th IEEE Int. Conf. Comput. Vis. ICCV*, Jul. 2001, pp. 480–487.

[4] S. Nam, Y. Hwang, Y. Matsushita, and S. J. Kim, "A holistic approach to cross-channel image noise modeling and its application to image denoising," in *Proc. IEEE Conf. Comput. Vis. Pattern Recognit. (CVPR)*, Jun. 2016, pp. 1683–1691.

[5] L. Shao, R. Yan, X. Li, and Y. Liu, "From heuristic optimization to dictionary learning: A review and comprehensive comparison of image denoising algorithms," *IEEE Trans. Cybern.*, vol. 44, no. 7, pp. 1001–1013, Jul. 2014.

[6] A. Foi, M. Trimeche, V. Katkovnik, and K. Egiazarian, "Practical poissonian-Gaussian noise modeling and fitting for single-image raw-data," *IEEE Trans. Image Process.*, vol. 17, no. 10, pp. 1737–1754, Oct. 2008.

[7] F. Luisier, T. Blu, and M. Unser, "Image denoising in mixed Poisson–Gaussian noise," *IEEE Trans. Image Process.*, vol. 20, no. 3, pp. 696–708, Mar. 2011.

[8] M. J. Black, G. Sapiro, D. H. Marimont, and D. Heeger, "Robust anisotropic diffusion," *IEEE Trans. Image Process.*, vol. 7, no. 3, pp. 421–432, Mar. 1998.

[9] C. Tomasi and R. Manduchi, "Bilateral filtering for gray and color images," in *Proc. 6th Int. Conf. Comput. Vis.*, Jan. 1998, pp. 836–846.

[10] A. Buades, B. Coll, and J.-M. Morel, "A non-local algorithm for image denoising," in *Proc. IEEE Comput. Soc. Conf. Comput. Vis. Pattern Recognit. (CVPR)*, Jun. 2005, pp. 60–65.

[11] K. Dabov, A. Foi, V. Katkovnik, and K. Egiazarian, "Image denoising by sparse 3-D transform-domain collaborative filtering," *IEEE Trans. Image Process.*, vol. 16, no. 8, pp. 2080–2095, Aug. 2007.

[12] K. Zhang, W. Zuo, Y. Chen, D. Meng, and L. Zhang, "Beyond a Gaussian denoiser: Residual learning of deep CNN for image denoising," *IEEE Trans. Image Process.*, vol. 26, no. 7, pp. 3142–3155, Jul. 2017.

[13] T. Remez, O. Litany, R. Giryes, and A. M. Bronstein, "Class-aware fully convolutional Gaussian and Poisson denoising," *IEEE Trans. Image Process.*, vol. 27, no. 11, pp. 5707–5722, Nov. 2018.

[14] T. Plotz and S. Roth, "Benchmarking denoising algorithms with real photographs," in *Proc. IEEE Conf. Comput. Vis. Pattern Recognit. (CVPR)*, Jul. 2017, pp. 1586–1595.

[15] C. Liu, W. T. Freeman, R. Szeliski, and S. B. Kang, "Noise estimation from a single image," in *Proc. IEEE Conf. Comput. Vis. Pattern Recognit.*, vol. 1, Jun. 2006, pp. 901–908.

[16] G. Petschnigg, R. Szeliski, M. Agrawala, M. Cohen, H. Hoppe, and K. Toyama, "Digital photography with flash and no-flash image pairs," *ACM Trans. Graph.*, vol. 23, no. 3, p. 664, Aug. 2004.

[17] C. Chen, Q. Chen, J. Xu, and V. Koltun, "Learning to see in the dark," in *Proc. IEEE/CVF Conf. Comput. Vis. Pattern Recognit.*, Jun. 2018, pp. 3291–3300.

[18] X. Guo, Y. Li, and H. Ling, "LIME: Low-light image enhancement via illumination map estimation," *IEEE Trans. Image Process.*, vol. 26, no. 2, pp. 982–993, Feb. 2017.

[19] C. Godard, K. Matzen, and M. Uyttendaele, "Deep burst denoising," in *Proc. Eur. Conf. Comput. Vis.*, Sep. 2018, pp. 538–554.

[20] T. Rabie, "Adaptive hybrid mean and median filtering of high-ISO long-exposure sensor noise for digital photography," *J. Electron. Imag.*, vol. 13, no. 2, p. 264, Apr. 2004.

[21] M. Zhang and B. K. Gunturk, "Multiresolution bilateral filtering for image denoising," *IEEE Trans. Image Process.*, vol. 17, no. 12, pp. 2324–2333, Dec. 2008.

[22] Y.-I. Pyo, R.-H. Park, and S. Chang, "Noise reduction in high-ISO images using 3-D collaborative filtering and structure extraction from residual blocks," *IEEE Trans. Consum. Electron.*, vol. 57, no. 2, pp. 687–695, May 2011.

[23] J. Xu, L. Zhang, and D. Zhang, "A trilateral weighted sparse coding scheme for real-world image denoising," in *Proc. Eur. Conf. Comput. Vis.*, Sep. 2018, pp. 20–36.

[24] J. J. Koenderink, "The structure of images," *Biological*, vol. 50, no. 5, pp. 363–370, 1984.

[25] H. Xu, C. Lu, R. Berendt, N. Jha, and M. Mandal, "Automatic nuclei detection based on generalized Laplacian of Gaussian filters," *IEEE J. Biomed. Health Informat.*, vol. 21, no. 3, pp. 826–837, May 2017.

[26] Z. Wang, "A new approach for segmentation and quantification of cells or nanoparticles," *IEEE Trans. Ind. Informat.*, vol. 12, no. 3, pp. 962–971, Jun. 2016.

[27] H. Kong, S. E. Sarma, and F. Tang, "Generalizing Laplacian of Gaussian filters for vanishing-point detection," *IEEE Trans. Intell. Transp. Syst.*, vol. 14, no. 1, pp. 408–418, Mar. 2013.

[28] X. Liu, L. Xie, B. Zhong, J.-X. Du, and Q. Peng, "Automatic facial flaw detection and retouching via discriminative structure tensor," *IET Image Process.*, vol. 11, no. 11, pp. 1068–1076, Nov. 2017.

[29] T. Lindeberg, "Feature detection with automatic scale selection," *Int. J. Comput. Vis.*, vol. 30, no. 2, pp. 79–116, 1998.

[30] E. Breen, G. Joss, and K. Williams, "Locating objects of interest within biological images: The top hat box filter," *J. Comput.-Assist. Microsc.*, vol. 3, no. 2, pp. 97–102, 1991.

[31] M. Zhang, T. Wu, and K. M. Bennett, "Small blob identification in medical images using regional features from optimum scale," *IEEE Trans. Biomed. Eng.*, vol. 62, no. 4, pp. 1051–1062, Apr. 2015.

[32] T. Lindeberg, "Edge detection and ridge detection with automatic scale selection," *Int. J. Comput. Vis.*, vol. 30, no. 2, pp. 117–156, Nov. 1998.

[33] A. Helman, *The Finest Peaks-Prominence Other Mountain Measures*. Bloomington, IN, USA: Trafford Publishing, 2005.

[34] J. Xu, L. Zhang, D. Zhang, and X. Feng, "Multi-channel weighted nuclear norm minimization for real color image denoising," in *Proc. IEEE Int. Conf. Comput. Vis. (ICCV)*, Oct. 2017, pp. 1105–1113.

[35] G. Wang, C. Lopez-Molina, and B. De Baets, "Blob reconstruction using unilateral second order Gaussian kernels with application to high-ISO long-exposure image denoising," in *Proc. IEEE Int. Conf. Comput. Vis. (ICCV)*, Oct. 2017, pp. 4817–4825.

[36] R. Hui and M. O'Sullivan, *Fiber Optic Measurement Techniques*. New York, NY, USA: Academic, 2009.

[37] T. Brooks, B. Mildenhall, T. Xue, J. Chen, D. Sharlet, and J. T. Barron, "Unprocessing images for learned raw denoising," in *Proc. IEEE/CVF Conf. Comput. Vis. Pattern Recognit. (CVPR)*, Jun. 2019, p. 11.

[38] A. O. Akyüz and E. Reinhard, "Noise reduction in high dynamic range imaging," *J. Vis. Commun. Image Represent.*, vol. 18, no. 5, pp. 366–376, Oct. 2007.

[39] L. Azzari, L. R. Borges, and A. Foi, "Modeling and estimation of signal-dependent and correlated noise," in *Denoising Photographic Images Video*. Cham, Switzerland: Springer, 2018, pp. 1–36.

[40] P. Chatterjee, N. Joshi, S. B. Kang, and Y. Matsushita, "Noise suppression in low-light images through joint denoising and demosaicing," in *Proc. CVPR*, Jun. 2011, pp. 321–328.

[41] S. Guo, Z. Yan, K. Zhang, W. Zuo, and L. Zhang, "Toward convolutional blind denoising of real photographs," in *Proc. IEEE/CVF Conf. Comput. Vis. Pattern Recognit. (CVPR)*, Jun. 2019, pp. 1712–1722.

[42] D. Marr and E. Hildreth, "Theory of edge detection," *Proc. Roy. Soc. London. B, Biol. Sci.*, vol. 207, pp. 187–217, Feb. 1980.

[43] L. Vincent, "Morphological grayscale reconstruction in image analysis: Applications and efficient algorithms," *IEEE Trans. Image Process.*, vol. 2, no. 2, pp. 176–201, Apr. 1993.

[44] S. Diciotti, S. Lombardo, G. Coppini, L. Grassi, M. Falchini, and M. Mascalchi, "The *LoG* characteristic scale: A consistent measurement of lung nodule size in CT imaging," *IEEE Trans. Med. Imag.*, vol. 29, no. 2, pp. 397–409, Feb. 2010.

[45] T. Lindeberg, "Image matching using generalized scale-space interest points," *J. Math. Imag. Vis.*, vol. 52, no. 1, pp. 3–36, May 2015.

[46] H. Kong, H. C. Akakin, and S. E. Sarma, "A generalized Laplacian of Gaussian filter for blob detection and its applications," *IEEE Trans. Cybern.*, vol. 43, no. 6, pp. 1719–1733, Dec. 2013.

[47] T. Lindeberg, "Detecting salient blob-like image structures and their scales with a scale-space primal sketch: A method for focus-of-attention," *Int. J. Comput. Vis.*, vol. 11, no. 3, pp. 283–318, Dec. 1993.

[48] I. Smal, M. Loog, W. Niessen, and E. Meijering, "Quantitative comparison of spot detection methods in fluorescence microscopy," *IEEE Trans. Med. Imag.*, vol. 29, no. 2, pp. 282–301, Feb. 2010.

[49] G. Wang, C. Lopez-Molina, G. Vidal-Diez de Ulzurrun, and B. De Baets, "Noise-robust line detection using normalized and adaptive second-order anisotropic Gaussian kernels," *Signal Process.*, vol. 160, pp. 252–262, Jul. 2019.

[50] G. Wang, C. Lopez-Molina, and B. De Baets, "Multiscale edge detection using first-order derivative of anisotropic Gaussian kernels," *J. Math. Imag. Vis.*, vol. 61, no. 8, pp. 1096–1111, Oct. 2019.

[51] D.-A. Huang, L.-W. Kang, Y.-C.-F. Wang, and C.-W. Lin, "Self-learning based image decomposition with applications to single image denoising," *IEEE Trans. Multimedia*, vol. 16, no. 1, pp. 83–93, Jan. 2014.
[52] G. Ghimpeteanu, T. Batard, M. Bertalmio, and S. Levine, "A decomposition framework for image denoising algorithms," *IEEE Trans. Image Process.*, vol. 25, no. 1, pp. 388–399, Jan. 2016.
[53] Y. Ren, Z. Ying, T. H. Li, and G. Li, "LECARM: low-light image enhancement using the camera response model," *IEEE Trans. Circuits Syst. Video Technol.*, vol. 29, no. 4, pp. 968–981, Apr. 2019.
[54] Z. Liu, L. Yuan, X. Tang, M. Uyttendaele, and J. Sun, "Fast burst images denoising," *ACM Trans. Graph.*, vol. 33, no. 6, pp. 1–9, Nov. 2014.

Gang Wang received the Ph.D. degree from Ghent University, Belgium, in 2019. He is currently a Research Assistant Professor with the Academy of Military Medical Sciences, China. His research interests include image processing, computer vision, machine learning, and brain-inspired visual perception.

Carlos Lopez-Molina received the Ph.D. degree from the Universidad Pública de Navarra in 2012. He is currently an Assistant Professor with the Universidad Pública de Navarra. His research interests are in low-level feature extraction/treatment for computer vision and automated bioimagery processing. He has developed most of his work around edge and boundary detection and in soft computing techniques for computer vision.

Bernard De Baets holds an M.Sc. degree in Maths (1988), a Postgraduate degree in Knowledge Technology (1991) and a Ph.D. degree in Maths (1995), all *summa cum laude* from Ghent University (Belgium). He is a Senior Full Professor in Applied Maths (1999) at Ghent University, where he is leading KERMIT, the Research Unit Knowledge-Based Systems. His publications comprise more than 500 articles in international journals and about 60 book chapters. He is a Government of Canada award holder (1988), an Honorary Professor of Budapest Tech (2006), an IFSA Fellow (2011), an Honorary Doctor of the University of Turku (2017), a Profesor Invitado of the Universidad Central "Marta Abreu" de las Villas (2017), and a Professor Extraordinarius of the University of South Africa (2019). He serves on the editorial boards of various international journals, in particular as Co-Editor-In-Chief of *Fuzzy Sets and Systems*.